Nano Research
2022, 15(5): 3971–3979

ISSN 1998-0124 CN 11-5974/O4
https://doi.org/10.1007/s12274-022-4084-1

Research Article

N-doped CNTs capped with carbon layer armored CoFe alloy as highly stable bifunctional catalyst for oxygen electrocatalysis

Bin Wang[1,§], Katam Srinivas[1,§], Yanfang Liu[1,§], Dawei Liu[1], Xiaojuan Zhang[1], Wanli Zhang[1], and Yuanfu Chen[1,2] (✉)

[1] *State Key Laboratory of Electronic Thin Films and Integrated Devices, University of Electronic Science and Technology of China, Chengdu 610054, China*
[2] *College of Science, and Institute of Oxygen Supply, Tibet University, Lhasa 850000, China*
[§] *Bin Wang, Katam Srinivas, and Yanfang Liu contributed equally to this work.*

Received: 15 November 2021 / **Revised:** 1 December 2021 / **Accepted:** 19 December 2021

ABSTRACT

Designing and fabricating the bifunctional electrocatalysts for the oxygen reduction reaction (ORR) and oxygen evolution reaction (OER) has long posed an uphill and pressing task for the interconversion of electricity and chemicals. Baring this in mind, herein, we propose a novel hierarchical nanoarchitecture of N-doped carbon nanotubes capped with carbon layer armored CoFe alloy (CoFe@NC-NT), which is facilely fabricated by spray drying and subsequent annealing process. As a bifunctional electrocatalyst, the well-designed CoFe@NC-NT shows a remarkably low overpotential of 257 mV and a half-wave potential of 0.74 V to obtain 10 mA·cm^{-2} in OER and ORR, respectively. Meanwhile, it is also characterized by exceptional operating stability to meet practical application for Zn-air batteries. The high catalytic activity of CoFe@NC-NT is attributed to the tight contact between the highly conductive nanotubes and metal alloy nanoparticles. And the qualified stability is ascribed to the coating effect of carbon layer shell to alloy core. Given the unique structural evolution with enhanced oxygen-involved reaction activity, we believe that this work can provide an appealing innovative approach towards the directed self-assembly of functional nanostructures to realize satisfying overall performance.

KEYWORDS

oxygen electrocatalysis, metal alloy, coating effect, self-assembly, Zn-air battery

1 Introduction

The interconversion of electricity and chemicals through electrocatalytic reaction is vitally important for renewable-energy initiatives such as metal-air battery. Designing and fabricating the high-efficiency electrocatalysts for the oxygen reduction reaction (ORR) and oxygen evolution reaction (OER) with sluggish kinetics has long posed an uphill and pressing task in this field [1, 2]. Commercial Pt/C and RuO_2 are respectively considered as benchmark catalysts for ORR and OER but have long been criticized for their insufficient durability [3, 4]. Recently, noble metal alloys (e.g., PdMo [5], AgPd [6], PtPd [7]) have constantly been reported as electrocatalysts with optimal Sabatier principle and exceptional stability benefited from the alloying effect. However, the scarcity is still a factor that cannot be ignored to limit the large-scale practical application for precious metal-based catalysts.

Recent studies [8, 9] including our previous work [10] have shown that transition metal-based alloys present high oxygen-involving electrocatalytic activity modulated by the optimal d band center for the appropriate bending energy. Besides, the oxyphilic oxidation state components of metal elements tend to be reduced in the alloying process [5, 11]. So, the stability of alloy catalysts can be improved, but notwithstanding, only to a limited extent. Toward this end, metal alloys moiety adsorbed onto or embedded into highly conductive solid matrixes have been widely reported as a protocol to generate a supported metallic catalyst with enhanced oxygen electrocatalysis and operation stability [12, 13]. Then, the proposed strategy of packaging metal alloys within the confined space of flexible graphene layers could effectively prevent the corrosion of metal species from a harsh environment [14]. However, the deactivation effect will be inevitably caused by their inadequate interaction strength and the obstruction of electron transfer from the inner metals to the out-layer carbon under the thick staked graphene layers. Analogously, some ingenious studies about encapsulating metal alloys into the cavity of carbon nanotubes (CNTs) was put forward, in which the activity and stability can be simultaneously promoted through the synergism of anisotropic CNTs and protection from carbon tube wall [15, 16]. Nevertheless, due to incompatible geometry, the limited surface contact (point to face) between metal alloy particles and the inner wall of the carbon support leads to the limited stimulation for the overall catalytic activity.

Encouraged by the outlined issues, we conceived a hierarchical nanoarchitecture consists of several individual functional units constructed by analogous self-assembly behavior could be an ideal solution to achieve the balance between full utilization of active sites and maintain its high stability. Herein, we employed a facile spray drying followed by high temperature annealing method to synthesize *in-situ* generated carbon nanotubes grafted with carbon layer encapsulated core-shell CoFe alloy nanoparticles (CoFe@NC-

Address correspondence to yfchen@uestc.edu.cn

NT). Through the systematic investigation, we found that the coexistence of Co and Fe species is the appropriate condition for the *in-situ* catalytic evolution of the unique nanoarchitecture. Specifically, the fast carburization of Fe species results in core-shell structure of carbon coated CoFe alloy, while the *in-situ* catalyzed precipitation of carbon source was activated by Co species and the obtained porous carbon eventually evolved into nanotubes. Interestingly, these two processes occurred simultaneously enables carbon layer encapsulated CoFe nanoparticle end-capped on carbon nanotube. Due to the unique structural features, CoFe@CN-NT catalyst manifested an outstanding OER (overpotencial is 257 mV vs. RHE; Tafel slope is 43.7 $mV{\cdot}dec^{-1}$), ORR (half-wave potential is 0.74 V vs. RHE; Tafel slope is 83.0 $mV{\cdot}dec^{-1}$) performance along with exceptional operation stability (132 h chronoamperometric test). Combining the robust and high-activity oxygen evolution and reduction catalysis, the CoFe@NC-NT was additionally selected as air-diffusion electrode for realizing rechargeable Zn-air battery. This work can provide an appealing innovative approach towards the directed self-assembly of functional nanostructures to realize satisfying overall performance.

2 Experimental methods

2.1 Preparation of the catalysts

The PANI/Zn-CoFe-PBA hybrid was synthesized as follows: 2 g polyaniline (PANI) powder was dispersed in DI water (500 mL) and ultrasonicated for at least 120 min. Then, 25 mmol zinc nitrate hexahydrate was dissolved in the as-obtained suspension to form solution **A**. Meanwhile, 12.5 mmol potassium hexacyanocobaltate and 12.5 mmol potassium ferricyanide were dissolved in DI water (500 mL) to prepare solution **B**. Afterwards, the two-solutions were mixed with vigorous stirring and aged for 480 min. Subsequently, the as-obtained suspension was subjected to spray-drying technique with 500 $mL{\cdot}h^{-1}$ pumping rate, and the inlet and outlet temperatures of spray dryer were noticed to be 180 and 110 °C, respectively. Afterwards, the obtained dark gray solid sample was annealed in a quartz tube for 120 min at 800 °C under hydrogen-argon mixture atmosphere with a flow ratio of 1:8. All the catalysts prepared in this work and their related information are listed in Table 1.

2.2 Preparation of working-electrode

4 mg of as prepared electrocatalysts were dispersed in 1 mL of mixed water and ethanol solution with the volume ratio of 3:1 by ultrasonication (30 min). After which, 50 μL of Nafion solution was added to the above suspension and the ultrasonication was continued for additional 30 min. Finally, 5 μL of as-obtained catalyst ink was deposited on the glassy carbon electrode followed by drying at ambient temperature for the subsequent OER property tests. Analogously, the catalyst ink preparation for ORR test is same as described, but 10 μL catalyst ink was drop-casted on RDE and RRDE to check the ORR performance.

2.3 Aqueous Zn–air batteries assembly

Rechargeable Zn-Air battery was constructed in a 6 M KOH aqueous electrolyte consisting of 0.2 M $Zn(Ac)_2$. Polished zinc sheet was utilized as metal anode and the bifunctional electrocatalyst loaded carbon paper was employed as cathode.

3 Results and discussion

3.1 Structure, composition, and morphology

We demonstrate a spray drying followed by annealing process to synthesize hierarchical catalyst CoFe@NC-NT, as depicted in Fig. S1 in the Electronic Supplementary Material (ESM). From SEM images shown in Fig. S2 in the ESM, the obtained precursor (Zn-CoFe-PBA/PANI: Fig. S3 in the ESM) after spray drying were characterized with a morphology of irregular bulk attached with relatively smaller aggregated particles. After subsequent thermal processes, a specific morphology of carbon layer armored alloy nanoparticle end-capped on carbon nanotube was evolved.

The SEM image of CoFe@NC-NT (Fig. 1(a)) declares its tubular structure and the presence of nanoparticle at the axial ends of nanotube can be unambiguously detected. While the selected area electron diffraction (SAED) patterns (Fig. 1(b)) further reveal the existence of crystalline structure of metal alloy. The finer morphology of separated structure was provided in TEM images (Figs. 1(c) and 1(d)), in which the structural characteristics of nanoparticle directly assembled with nanotube can be observed. The feature of multi-walled cavity for nanotube and core-shell structure for nanoparticle can be clearly witnessed in the high-resolution TEM images (Figs. 1(d_1) and (d_2)). More specifically, (110) lattice plane with 0.2 nm lattice fringes (Fig. 1(e)) can be indexed and is matching well with the SAED analysis [17, 18]. Noteworthily, the discontinuous region of the lattice fringe (Figs. 1(e_1) and 1(e_2)) can be realized, which indicates the presence of crystal defects [19]. Notably, lots of studies [20, 21] have disclosed that defects are of great significance for boosting catalytic activity, and some research groups even focus on defect engineering to enhance the catalytic performance. Moreover, the inner core CoFe alloy nanoparticle is closely wrapped by a shell layer with the thickness of ~7 nm. The images of elemental mapping (Figs. 1(f)–1(i) and Fig. S4 in the ESM) disclose that the Co and Fe elements are homogeneously distributed in the particle, that additionally confirming the alloy structure of CoFe. Besides, the metallic Co^0 and Fe^0 species can also be indexed in the core-level Co 2p and Fe 2p XPS spectra of CoFe@NC-NT (Fig. S5 in the ESM) [10, 22–24].

Table 1 The list of catalysts prepared in this work

Catalyst	Precursor	Heat-treatment time (min)	Morphology
CoFe@NC-NT-30	PANI/Zn-CoFe-PBA	30	Nanoparticle/sheet
CoFe@NC-NT-60	PANI/Zn-CoFe-PBA	60	Nanoparticle capped nanotube
CoFe@NC-NT-120	PANI/Zn-CoFe-PBA	120	Nanoparticle capped nanotube
CoFe@NC-NT-240	PANI/Zn-CoFe-PBA	240	Nanoparticle capped nanotube
CoFe@NC-NB	Zn-CoFe-PBA	120	Nanoparticle
Co@NC-NB	PANI/Zn-Co-PBA	120	Pompon-like
Fe_3C -NB	PANI/Zn-Co-PBA	120	Core-shell nanoparticle
NC	PANI	120	Coralline

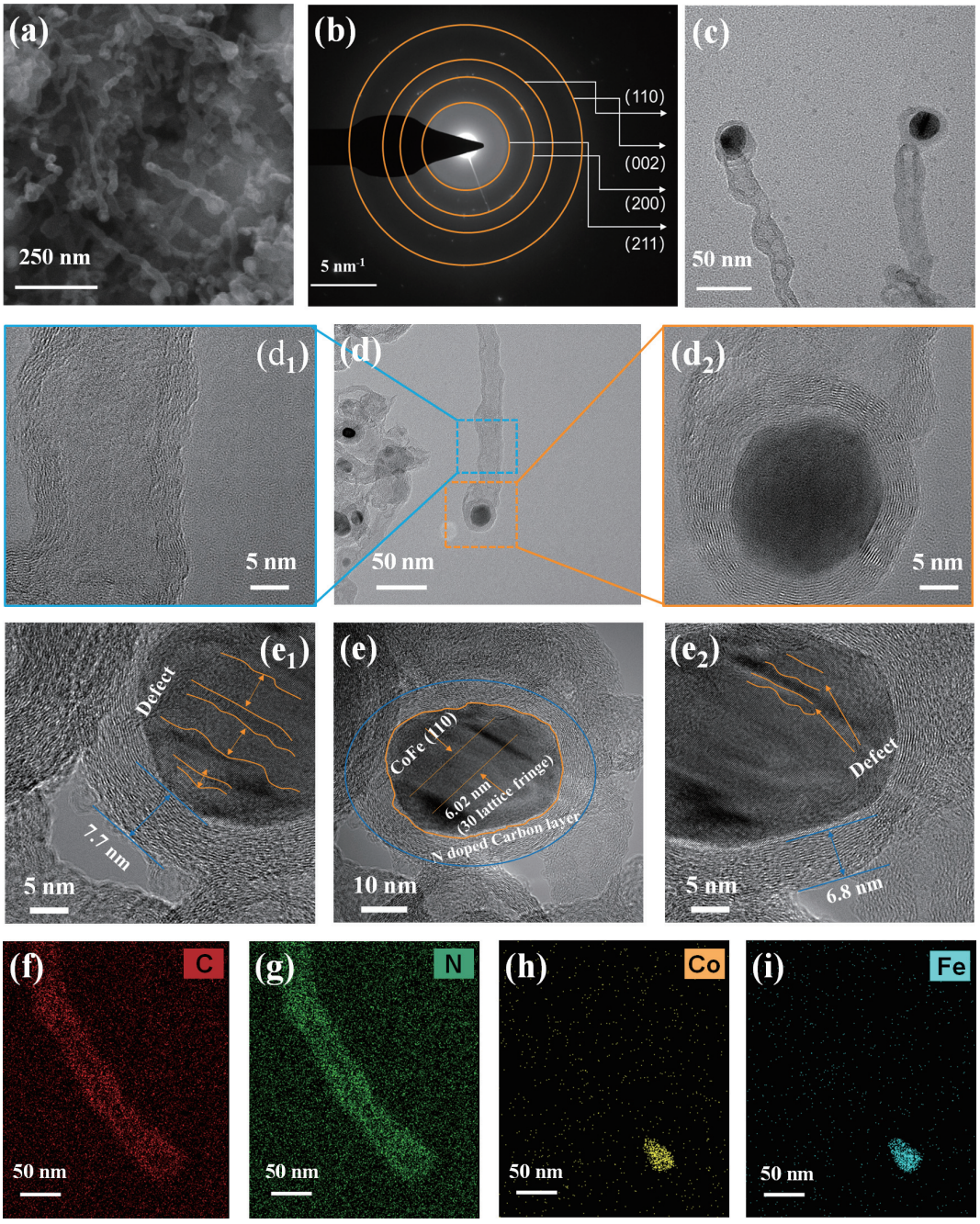

Figure 1 (a) SEM image, (b) SAED pattern, (c)–(e) TEM and HRTEM images, (f)–(i) elemental mapping of CoFe@NC-NT.

From a microstructure point of view, one-dimensional carbon nanotube is generally preferred in facilitating rapid O_2 and electrolyte diffusion throughout the whole catalysis process. While core-shell carbon coated alloy nanoparticle in favor of the maximum avoidance of environmental corrosion. Therefore, to elucidate the mechanism of the unique morphology evolution was essential and meaningful. In principle, the metal carbides *in-situ* generated in the decomposition process of carbon source accompanied with carburization tend to catalyze the precipitation of carbon and eventually evolve into nanotubes [25]. Hence, whether the specific morphology evolution was determined by the involvement of metal or not should be primarily clarified. Therefore, the thermally treated products (NC, Co@NC-NB, FeC@NC-NB, CoFe@NC-NB) of the raw PANI, Zn-Co-PBA/PANI, Zn-Fe-PBA/PANI and Zn-CoFe-PBA were characterized by SEM (Figs. 2(a)–2(h)) and the four samples can be respectively indexed as graphitized carbon, metallic Co, Fe_3C and CoFe alloy based on their XRD patterns (Figs. S6 and S7 in the ESM and Fig. 3(a)). SEM data disclosed the fact that the NC existed in a coralline-like micromorphology (Figs. 2(a) and 2(b)) rather than tubular structure, indicating that the specific CNT structure was hardly formed without the *in-situ* metal catalytic effect. However, the morphology of pyrolytic products (Co@NC-NB (Figs. 2(c) and 2(d)); Fe_3C@NC-NB (Figs. 2(e) and 2(f))) derived from metal-containing PBA/PANI hybrids are scarcely observed to be the microstructure like that of CoFe@NC-NT. Specifically, the Co@NC-NB shows a morphology of pompom with rough surfaces. Recent innovative research findings manifested that the presence of specific metals such as Co, Ni can catalyze the growth of nanotube-like structures on the surface of MOF crystals [26, 27]. We conclude that the morphology of nanospheres with rough surfaces for Co@NC-NB was essentially caused by the unmatured nanotubes under the negligible catalytic effect of Co for the deposition growth of carbon source. As for the Fe_3C@NC-NB, it tends to be existed in morphology of a core-shell particle structure accompanied by wrinkled nanosheets. It is

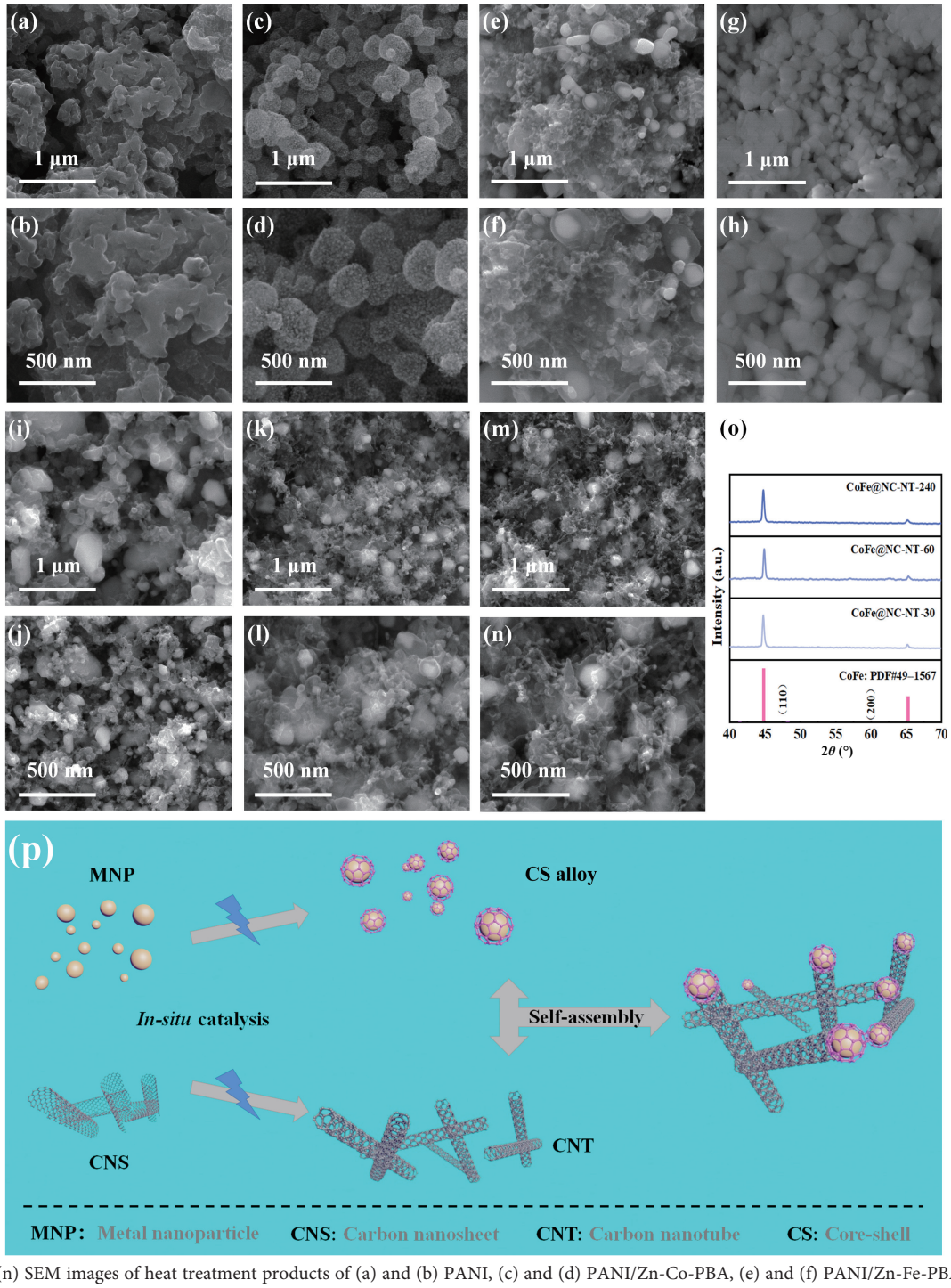

Figure 2 (a)–(n) SEM images of heat treatment products of (a) and (b) PANI, (c) and (d) PANI/Zn-Co-PBA, (e) and (f) PANI/Zn-Fe-PBA, and (g) and (h) Zn-CoFe-PBA under 800 °C. SEM images of heat treatment products of PANI/Zn-CoFe-PBA with different reaction time: 30 min (i) and (j), 60 min (k) and (l), 240 min (m) and (n) under 800 °C. (o) XRD patterns of CoFe@NC-NT-*X* (*X* denote reaction time). (p) Schematic of the morphology evolution for the CoFe@NC-NT catalyst.

plausible that the phase of Fe_3C could selectively promote the growth of carbon source into 2D nanosheet structure, which is totally different with the catalytic effect of Co. So far, we deduced that the PBA precursor containing both Co and Fe is the appropriate condition for the *in-situ* formation of nanotubes. Nonetheless, the nanotube microstructure was hardly observed in the thermally treated products of Zn-CoFe-PBA (Figs. 2(g) and 2(h)), possibly ascribed to the inadequate carbon source compared to the PANI/Zn-CoFe-PBA precursor.

To further ascertain the key role of reaction time on morphology evolution, the samples prepared at different time intervals (CoFe@CN-NT-*X*; *X* is the heat treatment time) have been examined by SEM analysis (Figs. 2(i)–2(n)) and their XRD patterns were provided in Fig. 2(o). Obviously, agglomerated particles can be observed in the SEM images of CoFe@CN-NT-30, instead of the morphology of core-shell nanoparticle inlaid on carbon nanotube. As the reaction time increases to 60 min, the above-mentioned tubular morphology peeped out from the dominant existing agglomerated particles, but the carbon nanotube length has been limited. When the reaction lasted for 120 min, the microscopic morphology of the CoFe@CN-NT-120 was mostly transformed into the specific morphology with a length of ~ 200 nm for the carbon nanotube. Moreover, there was no significant change in the microstructure as the reaction time continues to increase, as it was confirmed from that of CoFe@CN-NT-240 shown in Figs. 2(m) and 2(n).

Based on the above stated findings, we propose the concept of *in-situ* self-assembly morphology evolution for the CoFe@NC-NT catalyst, as depicted in Fig. 2(p). The PBA frameworks significantly shrink and fragment during thermal processes and eventually turn into core-shell CoFe alloy nanoparticles coated with carbon layers. Meanwhile, the PANI and PBA-derived porous carbon evolve into carbon nanotubes in the presence of bimetallic element (Co and Fe). It was presumed that both the aforementioned transformations were going on simultaneously and the *in-situ* generated carbon layers coated alloy nanoparticles occupied the corners of carbon nanotubes in order to evidence the core-shell nanoparticles inlaid nanotubes morphology.

Then, the Raman spectral data has been provided in Fig. 3(b), in which the characteristic D and G bands can be clearly observed and the CoFe@NC-NT displays the highest I_D/I_G value, suggesting the significant crystal defects [28]. The percentage of elements for the CoFe@NC-NT were further depicted in Fig. 3(c) based on the EDS analysis. The atom ratio of Fe and Co is close to 1:1 (confirmed by ICP-OES analysis Fig. S8 in the ESM), and the doped nitrogen element content is calculated to be 4.59%, which is of great significance for the enhancement of catalytic activity. Particularly, the oxygen catalysis is heavily relied on the types of N moieties and the more pyridinic nitrogen content is generally advantageous [29]. Additionally, the core-level N 1s XPS spectra of the catalysts were provided in Fig. 3(d) and the percentage of graphitic, pyrrolic and pyridinic nitrogen were depicted in Fig. S9 in the ESM. Obviously, a higher percentage of pyridinic N (59.1%) was contained in the CoFe@NC-NT sample compared to Co@NC-NB (47.8%) and Fe_3C-NB (57.1%), indicating its potential towards higher ORR activity, this can be confirmed in the discussion below. Moreover, the CoFe@NC-NT possesses ten times higher conductivity (44.961 μS·cm^{-1}) than that of Co@NC-NB (1.945 μS·cm^{-1}) and Fe_3C-NB (2.705 μS·cm^{-1}), as shown in the standard four-probe measurement (Fig. 3(e)), confirming the specific one-dimensional micromorphology possesses the shortest path to accelerate charge transport for catalytic process [30, 31]. In addition, the CoFe@NC-NT catalyst shows higher hydrophilicity with a contact angle compared with Co@NC-NB and Fe_3C-NB (Fig. 3(f) and Fig. S10 in the ESM). More importantly, the CoFe@NC-NT catalyst was characterized with higher specific surface area (88.44 m^2·g^{-1}) possessing hierarchical holes with wide size distribution, as depicted in Figs. 3(g) and 3(h). Notably, the great probabilities around 3.8 nm shown in the magnified version of micropores (Fig. S11 in the ESM) is most likely due to the pore formation during the gasification of Zn species [32].

3.2 Electrocatalytic oxygen evolution and reduction

All the as-prepared electrocatalysts have been homogeneously drop-casted onto the GC electrode (0.28 mg·cm^{-2} for OER, 0.10 mg·cm^{-2} for ORR) and considered them as the working electrodes to evaluate the oxygen catalysis performance in alkaline solution (1 M KOH for OER, 0.1 M KOH for ORR) under a constant ambient temperature of 25 °C.

Firstly, the samples (CoFe@NC-NT, Co@NC-NB, Fe_3C@NC-NB and commercial RuO_2) have been subjected to linear sweep voltammetry (LSV) tests to acquire polarization curves in OER process. According to Fig. 4(a) and Fig. S12 in the ESM, the CoFe@NC-NT catalyst displays an ultralow onset potential (217 mV at η_1) and overpotential (257 mV at η_{10} vs. RHE) with reference to the thermodynamic OER potential ($E^0_{H_2O/O_2}$ = 1.23 V), which are considerably smaller than those of Co@NC-NB (268, 339 mV), Fe_3C@NC-NB (248, 306 mV) and commercial RuO_2 (221, 295 mV). The catalytic kinetics of these catalysts was then assessed by Tafel plots (Fig. 4(b)). The resulting Tafel slope of

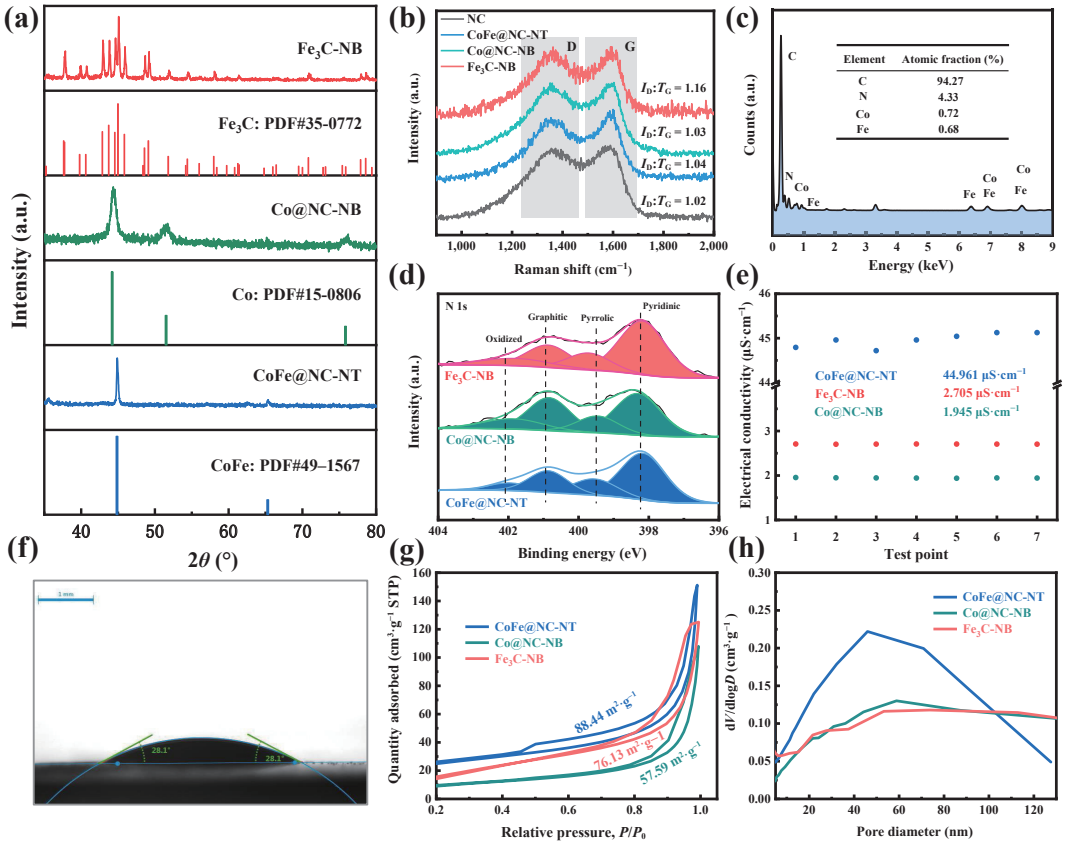

Figure 3 (a) XRD patterns of the CoFe@NC-NT, Co@NC-NB and Fe_3C-NB. (b) Raman spectra of the CoFe@NC-NT, Co@NC-NB, Fe_3C-NB and NC. (c) EDS spectrum of CoFe@NC-NT. (d) The high-resolution N 1s XPS spectra, (e) electrical conductivity of the CoFe@NC-NT, Co@NC-NB and Fe_3C-NB. (f) Contact angle measurement, (g) N_2 adsorption–desorption isotherms and (h) pore size distribution curves of CoFe@NC-NT.

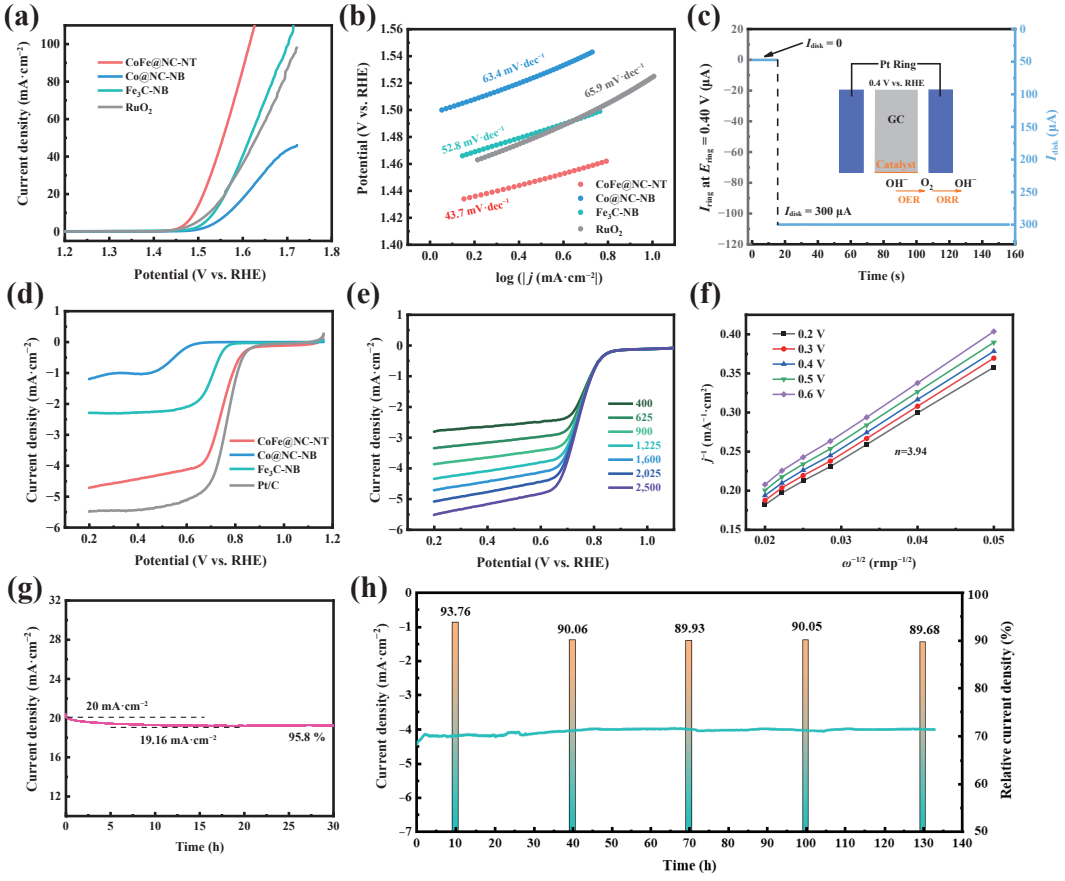

Figure 4 Catalytic performance of different catalysts for OER ((a)–(c) and (g)) and ORR ((d)–(f) and (h)). (a) and (d) Polarization curves. (b) and (e) Tafel plots of the CoFe@NC-NT, Co@NC-NB, Fe_3C-NB and commercial catalysts. (c) Evidence of generated O_2 using rotating ring disk electrode measurement (schematic shown as an inset). (f) K-L plots and ((g) and (h)) chronoamperometric test of the CoFe@NC-NT.

CoFe@NC-NT (43.7 mV·dec^{-1}) is much smaller than those of Co@NC-NB (63.4 mV·dec^{-1}), Fe_3C@NC-NB (52.8 mV·dec^{-1}) and commercial RuO_2 (65.9 mV·dec^{-1}), indicating its feasible reaction kinetics [33]. The further estimated largest double layer capacitance (C_{dl}) and smallest R_{ct} value of CoFe@NC-NT signify its possession of a relative higher electrochemical surface area and lower impedance (Figs. S13 and S14 in the ESM). Faradaic efficiency during catalytic process is one of the critical indicative performance factors to estimate the response aroused from OER or any other side reactions [34]. Thus, the rotating ring disk electrode (RRDE) test technique was employed to realize the Faradaic efficiency, in which a Pt ring electrode (at 400 mV vs. RHE) was used to recognize the O_2 signal from GC disk (Fig. 4(c), detailed measurement information see supplementary material). When a fixed current (300 μA) was applied to the disk electrode, a current of 109.4 μA was acquired on the Pt ring electrode (rotation speed = 1,600 rpm), signifying a high Faradaic efficiency (98.5%), and approving that the catalytic response was exclusively originated from water oxidation.

In addition to its promising OER activity, CoFe@NC-NT also shows potential ORR activity, as confirmed in Fig. S15 in the ESM. Then, the ORR catalytic performance of CoFe@NC-NT catalyst was further investigated by LSV in O_2-saturated alkaline electrolyte. The Co@NC-NB, Fe_3C@NC-NB and commercial Pt/C were also tested as control samples, as shown in (Fig. 4(d) and Fig. S16 in the ESM). Though there is a minor performance gap with commercial Pt/C, the CoFe@NC-NT shows more positive onset potential (E_{onset} is 1.14 V vs. RHE) and half-wave potential ($E_{1/2}$ is 0.74 V vs. RHE), compared with Co@NC-NB (0.74 and 0.54 V) and Fe_3C@NC-NB (1.18 and 0.70 V). The smaller Tafel slope obtained for CoFe@NC-NT (83.0 mV·dec^{-1}, Fig. S17 in the ESM) compared with other samples demonstrates the enhanced kinetics towards ORR application [35]. Selectivity is one of the key parameters to evaluate the activity of catalysts in ORR process in addition to catalytic performance, since O_2 can either be reduced by two electrons to produce H_2O_2 or by four electrons to yield H_2O [36]. Thus, rotating disk electrode (RDE) and rotating ring–disk electrode (RRDE) techniques were conducted to gain more insights into the number of electrons transferred per O_2 molecule (n). In RDE measurements, the current density of the CoFe@NC-NT originating from LSV exhibits a typical enhancement as the rotation speed escalated from 400 to 2,500 rpm, indicating its catalytic activity dependence on O_2 diffusion (Fig. 4(e)). Moreover, the n value for the CoFe@NC-NT was calculated to be 3.94 based on the Koutecky–Levich (K–L) plots (Fig. 4(f)), which suggests a four-electron pathway from O_2 to OH^-. Significantly, the almost parallel distribution and linearity of the K–L plots under applied potentials of 0.2–0.6 V suggests the similar numbers of electrons transfer during ORR process irrespective of applied potentials and endorse the first-order kinetics with respect to the dissolved O_2 concentration [37]. In RRDE measurements, the disk electrode has been scanned between 0.7 to 0.3 V, keeping the ring potential constant at 1.5 V to oxidize the H_2O_2 possibly produced during ORR back to O_2. Based on the detected real time current signal at the ring electrode and disk electrode, the 'n' value for CoFe@NC-NT is calculated to be ~3.89, and the H_2O_2 yield remained ~11.3% (Fig. S18 in the ESM), further confirming that the CoFe@NC-NT proceeds a four-electron pathway for ORR process.

Besides the exceptional catalytic activity, the CoFe@NC-NT catalyst showed satisfied stability during oxygen catalysis for its potential practical application. To be precise, its polarization curve

obtained after consecutive (1,000 for OER/5,000 for ORR) CV cycles almost overlapped with the initially obtained LSV plot, as observed in Figs. S19 and S20 in the ESM. Moreover, there is a slight attenuation exhibited in the chronoamperometric curve (Figs. 4(g) and 4(h), and Fig. S21 in the ESM), and the retention of current density is ~95.8% (~89.68%) after 30 h (132 h) of OER (ORR) operation. Moreover, The TEM images and LSV curves after electrocatalytic OER (Fig. S21 in the ESM) and ORR (Fig. S22 in the ESM) process have also been conducted, and the microstructure stability of the CoFe@NC-NT can be confirmed. In a proof-of-principle demonstration of its fuel cell application, we leveraged the bifunctional oxygen electrocatalytic activity of CoFe@NC-NT and used it as the cathode in an aqueous Zn–air battery (Fig. S23 in the ESM).

Overall, the proposed CoFe@NC-NT exhibited satisfied integrated catalytic performance compared with similar alloy-based catalysts reported in recent years, and the detailed information was listed in Table 2. We attribute the boosted catalytic activity and stability to its unique geometry and synergistic effect of composited species. Specifically, as for the head part (marked with pink dashed outline in Fig. 5) of the main catalyst body, (1) the intimate contact between metal alloy and carbon layer facilitates the electron transfer from the active metal core to the carbon layer and subsequently stimulates unique catalytic activity especially for OER process; (2) the alloy nanoparticles separately distributed in the sphere and the characteristic of hierarchical structure is beneficial to maximize the utilization of catalytic sites; (3) the carbon shell shields the inner alloy core from the harsh alkaline medium to ensure long-term stable catalysis. As for the tail part marked with orange dashed outline in Fig. 5; d (4) the *in-situ* derived N-doped CNTs act as the active sites contribute the most to the ORR process; (5) CNTs connected with carbon shell layers acts as fast channels for electronic transmission between electrolyte and the surface of catalyst. In a proof-of-principle demonstration of its fuel cell application, we leveraged the bifunctional oxygen electrocatalytic activity of CoFe@NC-NT and used it as the cathode in an aqueous Zn–air battery (Figs. S23 and S25 in the ESM). The assembled device displayed a better performance compared with the battery assembled with benchmark RuO_2 + Pt/C. The detailed analysis and discussion were provided in the supplementary materials.

Table 2 Related information about catalysts in this work and other similar reports

Catalyst	Morphology	Performance			Ref.
		OER (mV) (ORR (V))	ΔE (V)	Tafel slope OER (ORR)	
CoFe@NC-NT	Partical capped nanotube	257 (0.74)	0.74	43.7 (83.0)	This work
CoFe-Co_8FeS_8	Nanopartical	290 (/)	No mention	38.0 (/)	Previous work [10]
PdMo/C	Bimetallene	~ 470 (0.95)	~ 0.75	No mention	[5]
AgPd-Pd	Nanosheet	/ (0.85)	No mention	No mention	[6]
PtPdCo/C	Nanoring	~ 420 (0.97)	~ 0.68	No mention	[7]
NiCu/C	Nanopartical	400 (/)	No mention	80.0 (/)	[8]
NiFe/N-CNT	Partical in nanotube	290 (~ 0.75)	~ 0.77	79 (/)	[12]
Co@Graphene	Partical on nanosheet	383 (0.864)	0.75	47 (72)	[20]
NiFe@Graphene	Partical on nanosheet	290 (~ 0.8)	~ 0.72	43 (/)	[22]
FeCoNi@Graphene	Particle on nanotube	370 (~ 0.87)	~ 0.73	42 (118)	[25]
Co@CNT	Partical capped nanotube	231 (0.87)	0.591	93 (64)	[26]
FeCoNi/C	Nanosheet	343 (0.851)	0.722	82.4 (/)	[32]
Co@PC	Nanodot	/ (0.92)	No mention	/ (66)	[35]
NiFe@Graphite	Particle on nanosheet	210 (0.83)	0.61	62 (/)	[37]
Pd/Co_3O_4	Nanoparticle	410 (0.881)	0.625	No mention	[38]

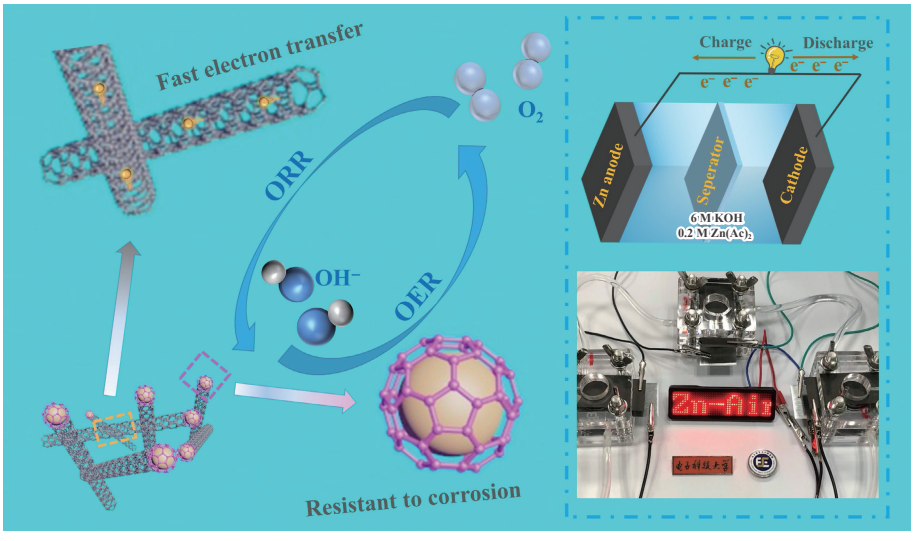

Figure 5 Schematic illustration of the CoFe@NC-NT and its application as cathode for Zn-air battery.

4 Conclusions

This work summarizes the development of N-doped carbon layer encapsulated CoFe alloy nanoparticles interconnected by carbon nanotubes (CoFe@NC-NT) as bifunctional oxygen electrocatalyst for zinc-air battery application. The systematic structural evolution analysis revealed that the Co and Fe species are essential in stimulating the *in-situ* catalytic growth of CNTs. The designed catalyst CoFe@NC-NT with distinct structural features, displays exceptional bifunctional activity towards oxygen evolution (η_{10} = 257 mV; Tafel slope = 43.7 mV·dec^{-1}) and reduction reactions ($E_{1/2}$ = 0.747 V; Tafel slope = 83.0 mV·dec^{-1}). In particular, the unique N-doped carbon layers protect the CoFe alloy nanoparticles from agglomeration during the catalysis process and thereby exhibits superior long-term operation abilities. Additionally, the derived one-dimensional CNTs can not only enhance the electrical conductivity but also improve the mechanical stability to the material in harsh alkaline environment. Besides, the abundant crystal defects aroused by the high N content (4.59%) act as catalytic active sites for boosting OER and ORR performance. Therefore, we believe that the proposed strategy for fabricating encapsulated alloy nanoparticles with interconnecting conductive moieties pave the path towards designing the advanced nanostructures for various energy conversion applications to alleviate the ever-increasing global energy crisis.

Acknowledgements

This research was supported by the National Natural Science Foundation of China (No. 21773024), Sichuan Science and Technology program (Nos. 2020YJ0324 and 2020YJ0262), Reformation and Development Funds for Local Region Universities from China Government in 2020 (No. ZCKJ 2020-11) and China Postdoctoral Science Foundation (No. 2019M653376).

Electronic Supplementary Material: Supplementary material is available in the online version of this article at https://doi.org/10.1007/s12274-022-4084-1.

References

[1] Gong, M.; Dai, H. J. A mini review of NiFe-based materials as highly active oxygen evolution reaction electrocatalysts. *Nano Res.* **2015**, *8*, 23–39.

[2] Chai, G. L.; Qiu, K. P.; Qiao, M.; Titirici, M. M.; Shang, C. X.; Guo, Z. X. Active sites engineering leads to exceptional ORR and OER bifunctionality in P, N Co-doped graphene frameworks. *Energy Environ. Sci.* **2017**, *10*, 1186–1195.

[3] Sun, J. Q.; Lowe, S. E.; Zhang, L. J.; Wang, Y. Z.; Pang, K. L.; Wang, Y.; Zhong, Y. L.; Liu, P. R.; Zhao, K.; Tang, Z. Y. et al. Ultrathin nitrogen-doped holey carbon@graphene bifunctional electrocatalyst for oxygen reduction and evolution reactions in alkaline and acidic media. *Angew. Chem., Int. Ed.* **2018**, *57*, 16511–16515.

[4] Wei, C.; Feng, Z. X.; Scherer, G. G.; Barber, J.; Shao-Horn, Y.; Xu, Z. J. Cations in octahedral sites: A descriptor for oxygen electrocatalysis on transition-metal spinels. *Adv. Mater.* **2017**, *29*, 1606800.

[5] Luo, M. C.; Zhao, Z. L.; Zhang, Y. L.; Sun, Y. J.; Xing, Y.; Lv, F.; Yang, Y.; Zhang, X.; Hwang, S.; Qin, Y. N. et al. PdMo bimetallene for oxygen reduction catalysis. *Nature* **2019**, *574*, 81–85.

[6] Luo, W. B.; Gao, X. W.; Chou, S. L.; Wang, J. Z.; Liu, H. K. Porous AgPd-Pd composite nanotubes as highly efficient electrocatalysts for lithium-oxygen batteries. *Adv. Mater.* **2015**, *27*, 6862–6869.

[7] Sun, Y. J.; Zhang, X.; Luo, M. C.; Chen, X.; Wang, L.; Li, Y. J.; Li, M. Q.; Qin, Y. N.; Li, C. J.; Xu, N. Y. et al. Ultrathin PtPd-based nanorings with abundant step atoms enhance oxygen catalysis. *Adv. Mater.* **2018**, *30*, 1802136.

[8] Ahsan, A.; Santiago, A. R. P.; Hong, Y.; Zhang, N.; Cano, M.; Rodriguez-Castellon, E.; Echegoyen, L.; Sreenivasan, S. T.; Noveron, J. C. Tuning of trifunctional NiCu bimetallic nanoparticles confined in a porous carbon network with surface composition and local structural distortions for the electrocatalytic oxygen reduction, oxygen and hydrogen evolution reactions. *J. Am. Chem. Soc.* **2020**, *142*, 14688–14701.

[9] Wang, Y. Y.; Kumar, A.; Ma, M.; Jia, Y.; Wang, Y.; Zhang, Y.; Zhang, G. X.; Sun, X. M.; Yan, Z. F. Hierarchical peony-like FeCo-NC with conductive network and highly active sites as efficient electrocatalyst for rechargeable Zn-air battery. *Nano Res.* **2020**, *13*, 1090–1099.

[10] Wang, B.; Hu, Y.; Yu, B.; Zhang, X. J.; Yang, D. X.; Chen, Y. F. Heterogeneous CoFe-Co_8FeS_8 nanoparticles embedded in CNT networks as highly efficient and stable electrocatalysts for oxygen evolution reaction. *J. Power Sources* **2019**, *433*, 126688.

[11] Li, Y. R.; Wang, Y.; Li, S. N.; Li, M. X.; Liu, Y. J.; Fang, X.; Dai, X. P.; Zhang, X. Pt_3Mn alloy nanostructure with high-index facets by Sn doping modified for highly catalytic active electro-oxidation reactions. *J. Catal.* **2021**, *395*, 282–292.

[12] Lei, H.; Wang, Z. L.; Yang, F.; Huang, X. Q.; Liu, J. H.; Liang, Y. Y.; Xie, J. P.; Javed, M. S.; Lu, X. H.; Tan, S. Z. et al. NiFe nanoparticles embedded N-doped carbon nanotubes as high-efficient electrocatalysts for wearable solid-state Zn-air batteries. *Nano Energy* **2020**, *68*, 104293.

[13] Ma, N.; Jia, Y.; Yang, X. F.; She, X. L.; Zhang, L. Z.; Peng, Z.; Yao, X. D.; Yang, D. J. Seaweed biomass derived (Ni, Co)/CNT nanoaerogels: Efficient bifunctional electrocatalysts for oxygen evolution and reduction reactions. *J. Mater. Chem. A* **2016**, *4*, 6376–6384.

[14] Yu, L.; Deng, D. H.; Bao, X. H. Chain mail for catalysts. *Angew. Chem., Int. Ed.* **2020**, *59*, 15294–15297.

[15] Zheng, X. J.; Deng, J.; Wang, N.; Deng, D. H.; Zhang, W. H.; Bao, X. H.; Li, C. Podlike N-doped carbon nanotubes encapsulating FeNi alloy nanoparticles: High-performance counter electrode materials for dye-sensitized solar cells. *Angew. Chem., Int. Ed.* **2014**, *53*, 7023–7027.

[16] Deng, J.; Ren, P. J.; Deng, D. H.; Yu, L.; Yang, F.; Bao, X. H. Highly active and durable non-precious-metal catalysts encapsulated in carbon nanotubes for hydrogen evolution reaction. *Energy Environ. Sci.* **2014**, *7*, 1919–1923.

[17] Chen, G. B.; Gao, R.; Zhao, Y. F.; Li, Z. H.; Waterhouse, G. I. N.; Shi, R.; Zhao, J. Q.; Zhang, M. T.; Shang, L.; Sheng, G. Y. et al. Alumina-supported CoFe alloy catalysts derived from layered-double-hydroxide nanosheets for efficient photothermal CO_2 hydrogenation to hydrocarbons. *Adv. Mater.* **2018**, *30*, 1704663.

[18] Wang, Y. Q.; Wang, H. G.; Ye, J. H.; Shi, L. Y.; Feng, X. Magnetic CoFe alloy@C nanocomposites derived from ZnCo-MOF for electromagnetic wave absorption. *Chem. Eng. J.* **2020**, *383*, 123096.

[19] Li, Y. L.; Liu, Q. L.; Zhang, S. Q.; Li, G. Q. The vital balance of graphitization and defect engineering for efficient bifunctional oxygen electrocatalyst based on N-doping carbon/CNT frameworks. *ChemCatChem* **2019**, *11*, 861–867.

[20] Wang, A. S.; Zhao, C. N.; Yu, M.; Wang, W. C. Trifunctional Co nanoparticle confined in defect-rich nitrogen-doped graphene for rechargeable Zn-air battery with a long lifetime. *Appl. Catal. B: Environ.* **2021**, *281*, 119514.

[21] Jiang, H.; Gu, J. X.; Zheng, X. S.; Liu, M.; Qiu, X. Q.; Wang, L. B.; Li, W. Z.; Chen, Z. F.; Ji, X. B.; Li, J. Defect-rich and ultrathin N doped carbon nanosheets as advanced trifunctional metal-free electrocatalysts for the ORR, OER and HER. *Energy Environ. Sci.* **2019**, *12*, 322–333.

[22] Khani, H.; Grundish, N. S.; Wipf, D. O.; Goodenough, J. B. Graphitic-shell encapsulation of metal electrocatalysts for oxygen evolution, oxygen reduction, and hydrogen evolution in alkaline solution. *Adv. Energy Mater.* **2020**, *10*, 1903215.

[23] Chen, Y.; Zhang, W. X.; Zhou, D.; Tian, H. J.; Su, D. W.; Wang, C. Y.; Stockdale, D.; Kang, F. Y.; Li, B. H.; Wang, G. X. Co-Fe mixed metal phosphide nanocubes with highly interconnected-pore architecture as an efficient polysulfide mediator for lithium-sulfur batteries. *ACS Nano* **2019**, *13*, 4731–4741.

[24] Wang, B.; Chen, Y. F.; Wang, X. Q.; Zhang, X. J.; Hu, Y.; Yu, B.;

Yang, D. X.; Zhang, W. L. A microwave-assisted bubble bursting strategy to grow Co_8FeS_8/CoS heterostructure on rearranged carbon nanotubes as efficient electrocatalyst for oxygen evolution reaction. *J. Power Sources* **2020**, *449*, 227561.

[25] Gupta, S.; Qiao, L.; Zhao, S.; Xu, H.; Lin, Y.; Devaguptapu, S. V.; Wang, X. L.; Swihart, M. T.; Wu, G. Highly active and stable graphene tubes decorated with FeCoNi alloy nanoparticles via a template-free graphitization for bifunctional oxygen reduction and evolution. *Adv. Energy Mater.* **2016**, *6*, 1601198.

[26] Xia, B. Y.; Yan, Y.; Li, N.; Wu, H. B.; Lou, X. W.; Wang, X. A metal-organic framework-derived bifunctional oxygen electrocatalyst. *Nat. Energy* **2016**, *1*, 15006.

[27] Pachfule, P.; Shinde, D.; Majumder, M.; Xu, Q. Fabrication of carbon nanorods and graphene nanoribbons from a metal-organic framework. *Nat. Chem.* **2016**, *8*, 718–724.

[28] Wang, B.; Chen, Y. F.; Wu, Q.; Lu, Y. J.; Zhang, X. J.; Wang, X. Q.; Yu, B.; Yang, D. X.; Zhang, W. L. A Co-coordination strategy to realize janus-type bimetallic phosphide as highly efficient and durable bifunctional catalyst for water splitting. *J. Mater. Sci. Technol.* **2021**, *74*, 11–20.

[29] Asset, T.; Atanassov, P. Iron-nitrogen-carbon catalysts for proton exchange membrane fuel cells. *Joule* **2020**, *4*, 33–44.

[30] Han, C.; Chen, Z.; Zhang, N.; Colmenares, J. C.; Xu, Y. J. Hierarchically CdS decorated 1D ZnO nanorods-2D graphene hybrids: Low temperature synthesis and enhanced photocatalytic performance. *Adv. Funct. Mater.* **2015**, *25*, 221–229.

[31] Wang, B.; Chen, Y. F.; Wang, X. Q.; Ramkumar, J.; Zhang, X. J.; Yu, B.; Yang, D. X.; Karpuraranjith, M.; Zhang, W. L. rGO wrapped trimetallic sulfide nanowires as an efficient bifunctional catalyst for electrocatalytic oxygen evolution and photocatalytic organic degradation. *J. Mater. Chem. A* **2020**, *8*, 13558–13571.

[32] Wang, H. F.; Chen, L. Y.; Wang, M.; Liu, Z.; Xu, Q. Hollow spherical superstructure of carbon nanosheets for bifunctional oxygen reduction and evolution electrocatalysis. *Nano Lett.* **2021**, *21*, 3640–3648.

[33] Liu, J. M.; Wang, C. B.; Sun, H. M.; Wang, H.; Rong, F. L.; He, L. H.; Lou, Y. F.; Zhang, S.; Zhang, Z. H.; Du, M. CoO_x/CoN_y nanoparticles encapsulated carbon-nitride nanosheets as an efficiently trifunctional electrocatalyst for overall water splitting and Zn-air battery. *Appl. Catal. B: Environ.* **2020**, *279*, 119407.

[34] Wang, B.; Wang, X. Q.; Wang, Z. G.; Srinivas, K.; Zhang, X. J.; Yu, B.; Yang, D. X.; Zhang, W. L.; Lau, T. C.; Chen, Y. F. Electronic modulation of NiS-PBA/CNT with boosted water oxidation performance realized by a rapid microwave-assisted *in-situ* partial sulfidation. *Chem. Eng. J.* **2021**, *420*, 130481.

[35] Zhou, T. P.; Shan, H.; Yu, H.; Zhong, C. A.; Ge, J. K.; Zhang, N.; Chu, W. S.; Yan, W. S.; Xu, Q.; Wu, H. A. et al. Nanopore confinement of electrocatalysts optimizing triple transport for an ultrahigh-power-density zinc-air fuel cell with robust stability. *Adv. Mater.* **2020**, *32*, 2003251.

[36] Liu, M. M.; Wang, L. L.; Zhao, K. N.; Shi, S. S.; Shao, Q. S.; Zhang, L.; Sun, X. L.; Zhao, Y. F.; Zhang, J. J. Atomically dispersed metal catalysts for the oxygen reduction reaction: Synthesis, characterization, reaction mechanisms and electrochemical energy applications. *Energy Environ. Sci.* **2019**, *12*, 2890–2923.

[37] Liu, P. T.; Gao, D. Q.; Xiao, W.; Ma, L.; Sun, K.; Xi, P. X.; Xue, D. S.; Wang, J. Self-powered water-splitting devices by core-shell NiFe@N-graphite-based Zn-air batteries. *Adv. Funct. Mater.* **2018**, *28*, 1706928.

[38] Seo, M. H.; Park, M. G.; Lee, D. U.; Wang, X. L.; Ahn, W.; Noh, S. H.; Choi, S. M.; Cano, Z. P.; Han, B.; Chen, Z. W. Bifunctionally active and durable hierarchically porous transition metal-based hybrid electrocatalyst for rechargeable metal-air batteries. *Appl. Catal. B: Environ.* **2018**, *239*, 677–687.